Appendix

1 PLATO Hand Specifications

1.1 Hardware Information

Table 1: Optimized linkage dimensions and PLATO Hand specifications.

Parameter	**Value**
Optimized linkage dimensions	
L_1	60.00 mm
L_2	30.00 mm
L_3	100.25 mm
L_4	20.50 mm
L_5	40.40 mm
PLATO Hand specifications	
Hand dimensions	23.5 cm × 18.3 cm × 12.7 cm
Total mass	1.3 kg
Degrees of freedom	8
Extended finger length	12 cm
Maximum payload	11.3 kg
Fingertip force	5–15 N
Operating voltage	24 V
Rated power	30 W
Rated torque (QDD)	0.43 N·m
Rated current (QDD)	1.4 A
Rated torque (servo)	0.82 N·m
Communication rate	CAN at 1 kHz (adjustable)

1.2 Software Information

Communication between the hand hardware and the host PC is implemented over a CAN bus. The QDD actuators communicate with the host PC through a PCAN-PCI Express FD interface, while the servo motors are handled separately through an OpenRB-150 microcontroller equipped with an Arduino MKR CAN Shield. The Aidin Miniature force/torque sensor is also integrated through the CAN communication pipeline and synchronized through ROS 2 topics at 100 Hz (fixed rate), allowing actuator states, distal force measurements, and controller commands to be processed within a unified software stack. To interface the hand with the ROS 2 Control framework [1], we implemented a custom ROS 2 Hardware Interface together with a joint-level impedance controller.

For each actuated joint, the commanded torque is computed as

$$\boldsymbol{\tau}_{\mathrm{cmd}} = \boldsymbol{\tau}_{\mathrm{ff}} + \mathbf{K}_p \left(\boldsymbol{q}_{\mathrm{des}} - \boldsymbol{q}\right) + \mathbf{K}_d \left(\dot{\boldsymbol{q}}_{\mathrm{des}} - \dot{\boldsymbol{q}}\right), \tag{1}$$

where $\boldsymbol{\tau}_{\text{ff}}$ is the feed-forward torque, $\boldsymbol{q}_{\text{des}}$ and $\dot{\boldsymbol{q}}_{\text{des}}$ are the desired joint position and velocity, $\boldsymbol{q}$ and $\dot{\boldsymbol{q}}$ are the measured joint position and velocity, and $\mathbf{K}_p$ and $\mathbf{K}_d$ denote the joint stiffness and damping gain matrices.

The QDD actuator control loop runs at 1 kHz. All joint-level control parameters can be updated online through ROS topics, including

- desired joint position $\boldsymbol{q}_{\text{des}}$,
- desired joint velocity $\dot{\boldsymbol{q}}_{\text{des}}$,
- stiffness gains $\mathbf{K}_p$,
- damping gains $\mathbf{K}_d$, and
- feed-forward torque $\boldsymbol{\tau}_{\text{ff}}$.

This interface allows the hand controller to operate as a low-level impedance layer while higher-level behaviors, including teleoperation commands and task-specific joint trajectories, are generated within the ROS 2 software stack.

For the servo-driven joints (joint 0 and joint 1), we use current-based position control rather than direct torque control. In this mode, the desired joint position is tracked by the embedded servo controller, while the effective joint stiffness is adjusted indirectly by limiting the maximum allowable motor current. In practice, we heuristically map the desired stiffness command to a current clamp to modulate virtual stiffness.

2 Experiments

2.1 Pullout Experiments

Figure 1: Index Pinch Pullout Configuration

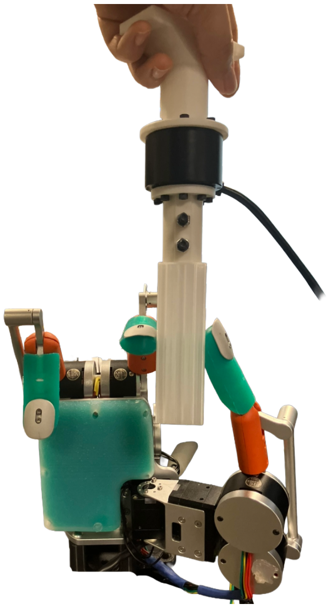

Figure 2: Lateral Pinch Pullout Configuration

All pull-out experiments were performed by a single author to reduce inter-operator variability. In total, 720 trials were collected across all fingertip conditions, surface geometries, and grasp types.

For each trial, the robotic hand was first moved to a predefined open joint configuration. A pinch grasp was then formed by applying a small closing offset to the joint configuration (approximately 0.2 in joint space) while simultaneously increasing the target impedance gains. In our setup, this procedure produced more stable and repeatable pinch formation than using direct torque control alone, since the object could otherwise shift relative to the fingertip before a consistent pinch state was established.

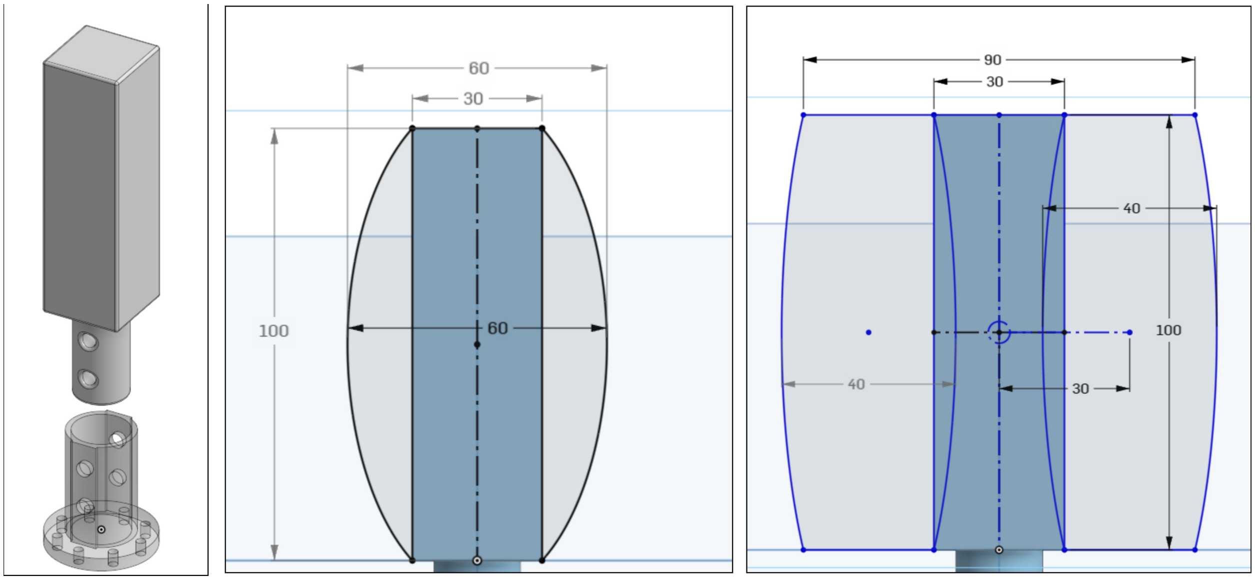

Figure 3: Object Mounting Interface and Curvature Dimension

For the pull-out experiments, the impedance gains were intentionally set high enough that grasping operated near the motor stall-current limit. We used this setting so that all fingertip conditions were compared under a similar actuation limit. In other words, the grasp force was effectively bounded by the same motor current saturation level across conditions, which made the comparison less sensitive to controller-dependent compliance and more reflective of the fingertip mechanics themselves. We found this to be a more consistent and fair comparison basis than using lower-gain impedance settings, which could introduce additional variation in the effective grasp stiffness.

The test object was mounted to a BOTA Rokubi force–torque sensor, and the experimenter manually pulled the object upward until grasp failure occurred. Only the Cartesian force measurements from the sensor were used in the analysis; torque measurements were not used in this study. During each trial, the object was pulled approximately upward, i.e., along the z-direction shown in the main text figure for the pull-out experiment. Because the pull-out motion was applied manually, care was taken to keep the pulling direction and pulling speed as consistent as possible across repetitions, with the pull applied approximately normal to the grasp plane.

Because the motors were operated near stall current during grasping, actuator temperature was continuously monitored throughout data collection. To prevent overheating and thermal bias, the experiment was paused whenever any motor temperature exceeded $70\,^{\circ}\mathrm{C}$, and the motors were allowed to cool before continuing the experiment. Also the sensor temperature was monitored during data collection and remained approximately within 30–$31\,^{\circ}\mathrm{C}$ throughout the experiments.

The task completion time for each trial was computed from the force measurement by identifying the start and end of the pull-out event using a threshold on the time derivative of the force signal. A small number of trials showing obvious measurement artifacts, such as abrupt nonphysical force spikes or corrupted sensor readings, were excluded from the analysis.

2.2 Force Sensing Experiments

For both the force sensitivity experiment and the contact force experiment, the robotic arm was controlled using the built-in controller provided by the Roboligent SDK. To ensure repeatable arm motion across trials, the arm was first manually backdriven through the desired motion using kinesthetic teaching, and the resulting joint trajectory was recorded. The same recorded joint trajectory was then replayed during the experiments.

For the force sensitivity experiment, the textured contact surface was fabricated by 3D printing a PLA model of a rock-like surface geometry. This provided a repeatable structured surface with spatially varying local features for contact-force transmission measurement.

To obtain an actuator-effort-based proprioceptive estimate, we first estimated motor torque from the measured q-axis motor current reported by the driver, together with an experimentally identified torque constant. This motor-torque estimate was then mapped through the finger transmission and linkage kinematics to estimate joint torque, and

Table 2: Pull-out experiment summary across fingertip conditions and surface geometries. Each entry reports mean ± standard deviation over $n = 30$ trials.

		Index pinch			Lateral pinch		
Surface	Condition	Force	F_z/F_{mag} (%)	Time (s)	Force	F_z/F_{mag} (%)	Time (s)
FLAT	NONE	12.16 ± 0.91	99.62 ± 0.30	4.05 ± 0.57	10.23 ± 1.14	99.32 ± 0.72	3.62 ± 0.40
	DP	16.56 ± 0.80	99.27 ± 0.20	4.34 ± 0.44	13.69 ± 1.06	99.35 ± 0.71	3.77 ± 0.49
	N	20.62 ± 1.10	99.49 ± 0.37	4.50 ± 0.54	12.46 ± 0.82	98.99 ± 0.68	3.73 ± 0.42
	DP+N	21.33 ± 0.61	99.81 ± 0.11	3.85 ± 0.47	25.92 ± 1.23	99.13 ± 0.76	3.62 ± 0.41
CONCAVE	NONE	10.97 ± 0.74	99.52 ± 0.46	4.24 ± 0.52	10.84 ± 1.19	99.39 ± 0.59	3.66 ± 0.43
	DP	17.11 ± 0.60	99.70 ± 0.18	4.47 ± 0.42	17.34 ± 0.81	99.40 ± 0.57	3.68 ± 0.43
	N	22.66 ± 0.90	99.14 ± 1.45	4.45 ± 0.41	18.21 ± 1.02	99.71 ± 0.08	3.42 ± 0.50
	DP+N	23.70 ± 0.69	99.30 ± 0.60	4.46 ± 0.34	24.45 ± 1.73	98.86 ± 0.88	4.07 ± 0.36
CONVEX	NONE	10.61 ± 1.06	99.46 ± 0.79	4.07 ± 0.53	11.59 ± 0.72	99.44 ± 0.45	3.69 ± 0.36
	DP	15.34 ± 1.70	99.57 ± 0.42	3.91 ± 0.54	15.92 ± 0.88	99.13 ± 0.28	3.66 ± 0.38
	N	22.35 ± 1.20	99.33 ± 0.49	4.21 ± 0.46	19.11 ± 0.78	99.63 ± 0.21	3.53 ± 0.35
	DP+N	23.63 ± 1.08	99.66 ± 0.37	3.81 ± 0.47	24.87 ± 0.71	99.73 ± 0.32	3.73 ± 0.35

the corresponding external contact force was inferred through the fingertip Jacobian. In this way, the proprioceptive estimate was derived entirely from actuator-side measurements and the hand kinematic model, while the distal force/torque sensor served as the reference measurement.

For the force traces shown in Fig. 6(b), we applied a scalar discrete-time Kalman filter for smoothing:

$$x_k = x_{k-1} + w_k, \qquad z_k = x_k + v_k,$$

where x_k is the latent smoothed force signal, z_k is the measured force signal, $w_k \sim \mathcal{N}(0, Q)$ is the process noise, and $v_k \sim \mathcal{N}(0, R)$ is the measurement noise. In our implementation, we used $Q = 10^{-5}$ and $R = 10^{-2}$.

2.3 Manipulation Experiments

For the manipulation experiments, the robotic arm was controlled using the Cartesian impedance controller provided by the Roboligent SDK and was teleoperated using a 3Dconnexion SpaceMouse

For edge-interaction tasks, including orange peeling, paper singulation, and lid opening, predefined joint impedance trajectories were assigned to SpaceMouse button inputs for the PLATO Hand. In these tasks, the operator teleoperated the arm to establish the desired contact configuration, after which the hand executed the corresponding predefined motion primitive through button-triggered commands.

For coin picking and card picking, proprioceptive force sensing was used to detect contact through a force threshold, which then triggered execution of a predefined joint impedance trajectory. This allowed the operator to rely on the intrinsic compliance of the fingers together with proprioceptive force feedback to perform the task more reliably and with less precise timing during teleoperation.

We also considered comparing against a version without proprioceptive force sensing. However, in practice, simply increasing the stiffness through higher K_p gains was not sufficient to eliminate compliance, because the system remained limited by the physical torque capability of the QDD actuators. As a result, even at the maximum feasible stiffness gains, passive compliance remained present, making a purely high-stiffness baseline less meaningful for isolating the effect of proprioceptive contact detection.

For card flipping, the operator first teleoperated the arm to achieve edge insertion, after which a predefined joint trajectory was executed through a SpaceMouse button input.

3 Hybrid Fingertip Model

This section develops a reduced-order mechanical model of the hybrid fingertip. The purpose of the model is not to reproduce every detail of real fingertip contact, but to isolate the structural mechanism that matters most for design. When the fingertip is pressed against an object, the imposed motion is not absorbed by a single deformation mode. Instead, part of it is accommodated by global bending of the fingertip structure, while the remainder appears as local indentation at the contact interface. The central question of the model is therefore how this imposed displacement is partitioned between those two modes.

This viewpoint is useful because the two deformation modes have very different consequences for manipulation. Global bending tends to dissipate motion within the fingertip structure itself, whereas local indentation more directly shapes the contact patch and force transmission. To capture this tradeoff in a simple and interpretable way, we model the fingertip body as a composite beam and the local interface using Hertzian indentation. These two ingredients are then combined through an energy-based formulation, yielding a design-oriented model that makes explicit how dorsal nail reinforcement and internal distal support shift deformation from global bending into local contact indentation.

3.1 Composite Beam Flexural Rigidity

To model bending of the hybrid fingertip, we treat the cross-section as a bonded composite beam consisting of three material components: the compliant pulp (p), the rigid fingernail (n), and the embedded distal phalanx (d). We assume small-strain Euler–Bernoulli bending and perfect bonding between materials, so that the cross-section remains kinematically compatible across the constituent layers. Because the distal phalanx is present only over the proximal portion of the fingertip, the beam is divided into two longitudinal segments. In the proximal segment ($0 \leq x \leq L_1$), all three components are present; in the distal segment ($L_1 < x \leq L$), the distal phalanx is absent.

We begin with the proximal segment. Let the pulp have width b_p and height h_p, the distal phalanx have width b_d and height h_d, and the fingernail have thickness h_n. We assume the nail spans the full pulp width, so that its cross-sectional area is $A_n = b_p h_n$. Since the distal phalanx occupies an embedded region within the pulp, the effective pulp area is modeled as the gross pulp rectangle minus the region occupied by the distal phalanx. The corresponding areas are

$$A_p = b_p h_p - b_d h_d, \tag{2}$$

$$A_d = b_d h_d, \tag{3}$$

$$A_n = b_p h_n. \tag{4}$$

The centroids of the gross pulp rectangle, distal phalanx region, and fingernail are

$$y_{\text{gross}} = \frac{h_p}{2}, \tag{5}$$

$$y_d = h_p - \frac{h_d}{2}, \tag{6}$$

$$y_n = h_p + \frac{h_n}{2}. \tag{7}$$

Here y is measured from the ventral side of the pulp cross-section, so the nail lies above the pulp and the distal phalanx is embedded eccentrically within it.

The centroid of the effective pulp region is obtained by subtracting the distal-phalanx occupied region from the gross pulp rectangle:

$$y_p = \frac{b_p h_p \, y_{\text{gross}} - b_d h_d \, y_d}{b_p h_p - b_d h_d} = \frac{b_p h_p \, y_{\text{gross}} - b_d h_d \, y_d}{A_p}. \tag{8}$$

The neutral axis of the proximal composite section is then given by the standard stiffness-weighted centroid formula,

$$\bar{y}_1 = \frac{E_p A_p y_p + E_d A_d y_d + E_n A_n y_n}{E_p A_p + E_d A_d + E_n A_n}, \tag{9}$$

where E_p, E_d, and E_n are the Young's moduli of the pulp, distal phalanx, and nail, respectively.

To compute the composite bending stiffness, we next evaluate the centroidal second moments of area of the individual components. For the distal phalanx and fingernail, these are

$$I_d^c = \frac{1}{12} b_d h_d^3, \tag{10}$$

$$I_n^c = \frac{1}{12} b_p h_n^3. \tag{11}$$

For the pulp, the effective cross-section is obtained by subtracting the distal-phalanx-occupied region from the gross pulp rectangle. Its centroidal second moment is therefore

$$I_p^c = \left[\frac{b_p h_p^3}{12} + b_p h_p \left(y_{\text{gross}} - y_p\right)^2\right] - \left[\frac{b_d h_d^3}{12} + b_d h_d \left(y_d - y_p\right)^2\right].$$

This expression applies the parallel axis theorem to both the gross pulp region and the embedded distal-phalanx region before subtraction, yielding the second moment of the effective pulp region about its own centroid.

The flexural rigidity of the proximal segment is then obtained by summing the stiffness contributions of all three materials relative to the composite neutral axis:

$$(EI)_1 = \sum_{k \in \{p,d,n\}} E_k \left[I_k^c + A_k (y_k - \bar{y}_1)^2\right], \tag{12}$$

where (y_p, y_d, y_n) denote the centroids of the effective pulp region, distal phalanx, and fingernail, respectively.

For the distal segment ($L_1 < x \leq L$), the distal phalanx is absent, so only the pulp and fingernail contributions are retained when computing the centroid, second moments, and flexural rigidity. This yields the distal-segment rigidity $(EI)_2$.

Thus, the fingertip is modeled as a piecewise beam with

$$EI(x) = \begin{cases} (EI)_1, & 0 \leq x \leq L_1, \\ (EI)_2, & L_1 < x \leq L. \end{cases} \tag{13}$$

This construction makes explicit how the fingernail and embedded distal phalanx modify the section mechanics. The fingernail shifts stiffness toward the dorsal surface, while the distal phalanx provides internal support within the pulp. Together, these features shift the neutral axis and increase the effective flexural rigidity of the fingertip.

3.2 Effective Rigidity from Energy Equivalence

The piecewise beam above is convenient for representing the hybrid structure, but the deformation-partitioning model in the main text is easier to analyze if the fingertip is represented by a single equivalent bending rigidity. We therefore define an effective flexural rigidity $(EI)_{\text{eff}}$ by requiring that a uniform cantilever with the same length and boundary condition store the same bending strain energy as the composite piecewise beam under the same tip load.

Consider a tip force F applied at $x = L$. The bending moment distribution is

$$M(x) = F(L - x). \tag{14}$$

The strain energy stored in the composite beam is

$$U_b^{\text{comp}} = \frac{1}{2}\left[\int_0^{L_1} \frac{M(x)^2}{(EI)_1}\, dx + \int_{L_1}^{L} \frac{M(x)^2}{(EI)_2}\, dx\right]. \tag{15}$$

Substituting $M(x) = F(L - x)$ gives

$$U_b^{\text{comp}} = \frac{F^2}{2}\left[\int_0^{L_1} \frac{(L-x)^2}{(EI)_1}\, dx + \int_{L_1}^{L} \frac{(L-x)^2}{(EI)_2}\, dx\right]. \tag{16}$$

Let $L_2 = L - L_1$. Then

$$\int_0^{L_1} (L-x)^2\, dx = \frac{L^3 - L_2^3}{3}, \tag{17}$$

$$\int_{L_1}^{L} (L-x)^2\, dx = \frac{L_2^3}{3}, \tag{18}$$

so that

$$U_b^{\mathrm{comp}} = \frac{F^2}{6}\left[\frac{L^3 - L_2^3}{(EI)_1} + \frac{L_2^3}{(EI)_2}\right]. \tag{19}$$

Now consider an equivalent uniform beam of length L and rigidity $(EI)_{\mathrm{eff}}$. Under the same tip force F, its bending strain energy is

$$U_b^{\mathrm{eff}} = \frac{F^2 L^3}{6(EI)_{\mathrm{eff}}}. \tag{20}$$

We define $(EI)_{\mathrm{eff}}$ by equating the two energies:

$$U_b^{\mathrm{eff}} = U_b^{\mathrm{comp}}. \tag{21}$$

Substituting the expressions above yields

$$\frac{F^2 L^3}{6(EI)_{\mathrm{eff}}} = \frac{F^2}{6}\left[\frac{L^3 - L_2^3}{(EI)_1} + \frac{L_2^3}{(EI)_2}\right]. \tag{22}$$

After canceling $F^2/6$, we obtain

$$(EI)_{\mathrm{eff}} = \frac{L^3}{\dfrac{L^3 - L_2^3}{(EI)_1} + \dfrac{L_2^3}{(EI)_2}}. \tag{23}$$

This equivalent rigidity is defined with respect to the tip-loaded cantilever case used in the present model. For a uniform cantilever under tip load F, the tip deflection is

$$\delta_b = \frac{F L^3}{3(EI)_{\mathrm{eff}}}. \tag{24}$$

Solving for F gives

$$F = \frac{3(EI)_{\mathrm{eff}}}{L^3}\,\delta_b. \tag{25}$$

The bending strain energy may then be written directly in terms of the tip deflection:

$$\begin{aligned} U_b(\delta_b) &= \frac{1}{2} F \delta_b \qquad (26) \\ &= \frac{1}{2}\,\frac{3(EI)_{\mathrm{eff}}}{L^3}\,\delta_b^2. \qquad (27) \end{aligned}$$

This is the bending-energy expression used in the main text.

3.3 Hertzian Contact Indentation

The composite-beam model above captures the *global* bending compliance of the fingertip structure. However, when the fingertip presses against an object, not all of the imposed deformation is accommodated by global bending. A second part of the deformation occurs *locally* at the contact interface, where the compliant pulp indents against the environment. To model this local deformation, we use a Hertzian contact approximation.

This choice is intentionally simplified. Our goal is not to reproduce every detail of real fingertip contact, which may involve large strains, viscoelasticity, friction, and geometry-dependent effects. Rather, we seek a reduced-order analytical model that relates local indentation to contact force, contact size, and stored elastic energy. This allows the contact contribution to be combined with the beam-bending model in a single design-oriented framework.

We model the pulp as an elastic half-space with effective modulus

$$E^* = \frac{E_p}{1 - \nu_p^2}, \tag{28}$$

where E_p is the Young's modulus of the pulp material and ν_p is its Poisson ratio. Let R_{eff} denote the effective contact radius determined by the curvatures of the fingertip and the environment.

Under Hertzian contact, the normal force associated with a local indentation depth δ_c is

$$F(\delta_c) = \frac{4}{3} E^* \sqrt{R_{\text{eff}}}\, \delta_c^{3/2}. \tag{29}$$

The corresponding contact radius is

$$a = \sqrt{R_{\text{eff}}\, \delta_c}. \tag{30}$$

Thus, larger local indentation increases both the contact force and the contact patch size.

The elastic energy stored in local indentation is obtained from the work done during compression:

$$\begin{aligned} U_c(\delta_c) &= \int_0^{\delta_c} F(\delta)\, d\delta \qquad (31) \\ &= \int_0^{\delta_c} \frac{4}{3} E^* \sqrt{R_{\text{eff}}}\, \delta^{3/2}\, d\delta \qquad (32) \\ &= \frac{4}{3} E^* \sqrt{R_{\text{eff}}} \int_0^{\delta_c} \delta^{3/2}\, d\delta \qquad (33) \\ &= \frac{4}{3} E^* \sqrt{R_{\text{eff}}} \left[\frac{2}{5} \delta^{5/2} \right]_0^{\delta_c}. \qquad (34) \end{aligned}$$

Therefore,

$$U_c(\delta_c) = \frac{8}{15} E^* \sqrt{R_{\text{eff}}}\, \delta_c^{5/2}. \tag{35}$$

This gives the local-contact energy term used in the deformation-partitioning model.

3.4 Lagrangian Formulation for Energy Minimization

We now combine the two reduced-order descriptions introduced above: the beam model for global fingertip bending and the Hertz model for local contact indentation. The purpose of this step is to obtain a single mechanistic model that explains how an imposed fingertip approach is distributed between *structural bending* and *local contact deformation*. This competition is the central phenomenon of interest in the present work.

The key modeling assumption is that when the fingertip is pressed against an object by a prescribed amount, the total approach displacement is not accommodated by a single deformation mode. Instead, part of the motion is absorbed by bending of the fingertip structure, while the remainder is absorbed by local indentation of the compliant pulp at the contact interface. We therefore decompose the total imposed displacement as

$$\delta_{\text{total}} = \delta_b + \delta_c, \tag{36}$$

where δ_b denotes the portion of deformation accommodated by global bending and δ_c denotes the portion accommodated by local contact indentation.

This decomposition gives the model its design relevance. If the fingertip is globally compliant, a larger fraction of the imposed displacement may be spent in bending before substantial local indentation develops. In contrast, if the fingertip is dorsally reinforced and resists bending, more of the same imposed displacement is redirected into local contact deformation. The latter case is desirable when the goal is to preserve concentrated contact, maintain a meaningful contact patch, and transmit interaction forces more directly through the fingertip.

The question, then, is how the pair (δ_b, δ_c) should be determined for a given imposed displacement δ_{total}. Rather than prescribing this partition heuristically, we determine it from an energy principle. Among all admissible pairs satisfying the compatibility condition above, we assume that the physically realized deformation is the one that minimizes the total stored elastic energy. In other words, the fingertip distributes deformation in the energetically most favorable way. This is simply the static equilibrium condition written in a form that makes the competition between the two deformation modes explicit.

The total elastic energy is written as

$$U_{\text{total}} = U_b(\delta_b) + U_c(\delta_c), \tag{37}$$

where the bending contribution is

$$U_b(\delta_b) = \frac{1}{2}\,\frac{3(EI)_{\text{eff}}}{L^3}\,\delta_b^2, \tag{38}$$

and the local contact contribution is

$$U_c(\delta_c) = \frac{8}{15}E^*\sqrt{R_{\text{eff}}}\,\delta_c^{5/2}. \tag{39}$$

The first term penalizes global bending, while the second penalizes local compression at the contact interface. The difficulty is that δ_b and δ_c cannot be chosen independently: whatever portion of the imposed displacement is not absorbed by bending must appear as local indentation, and vice versa. Thus, the minimization must be carried out subject to the compatibility condition

$$\delta_{\text{total}} = \delta_b + \delta_c.$$

To handle this constraint, we use a standard Lagrange multiplier formulation. Rather than minimizing the energy while enforcing the constraint separately, we introduce an auxiliary variable λ and incorporate the compatibility condition directly into the objective. In this role, λ enforces the requirement that the total imposed displacement be exactly partitioned between bending and contact indentation. This gives the Lagrangian

$$\mathcal{L}(\delta_b, \delta_c, \lambda) = U_b(\delta_b) + U_c(\delta_c) + \lambda\left(\delta_{\text{total}} - \delta_b - \delta_c\right), \tag{40}$$

whose minimizing solution gives the deformation partition that both satisfies the imposed total displacement and minimizes the total stored elastic energy.

To find this minimum-energy partition, we differentiate $\mathcal{L}$ with respect to each variable, namely δ_b, δ_c, and λ, and set the resulting expressions to zero. Intuitively, this means we look for the point at which a small change in bending, contact indentation, or the constraint variable can no longer reduce the total energy. This gives

$$\frac{\partial \mathcal{L}}{\partial \delta_b} = \frac{3(EI)_{\text{eff}}}{L^3}\delta_b - \lambda = 0, \tag{41}$$

$$\frac{\partial \mathcal{L}}{\partial \delta_c} = \frac{4}{3}E^*\sqrt{R_{\text{eff}}}\,\delta_c^{3/2} - \lambda = 0, \tag{42}$$

$$\frac{\partial \mathcal{L}}{\partial \lambda} = \delta_{\text{total}} - \delta_b - \delta_c = 0. \tag{43}$$

These equations can be interpreted directly. The compatibility condition ensures that the imposed displacement is exactly divided between bending and local indentation, while the other two equations show that the system cannot reduce its energy further by shifting a small amount of deformation from one mode to the other.

Eliminating the Lagrange multiplier gives

$$\frac{3(EI)_{\text{eff}}}{L^3}\delta_b = \frac{4}{3}E^*\sqrt{R_{\text{eff}}}\,\delta_c^{3/2}, \tag{44}$$

which shows directly that the bending response and contact response must balance one another. Substituting $\delta_b = \delta_{\text{total}} - \delta_c$ from the compatibility constraint yields

$$\frac{3(EI)_{\text{eff}}}{L^3}\left(\delta_{\text{total}} - \delta_c\right) = \frac{4}{3}E^*\sqrt{R_{\text{eff}}}\,\delta_c^{3/2}. \tag{45}$$

Rearranging,

$$\delta_{\text{total}} - \delta_c = \frac{4E^*\sqrt{R_{\text{eff}}}L^3}{9(EI)_{\text{eff}}}\,\delta_c^{3/2}. \tag{46}$$

Defining

$$\beta = \frac{4E^* \sqrt{R_{\text{eff}}} L^3}{9(EI)_{\text{eff}}}, \tag{47}$$

we obtain the scalar nonlinear equation

$$\delta_c + \beta\, \delta_c^{3/2} = \delta_{\text{total}}. \tag{48}$$

This reduced form is useful because it condenses the design tradeoff into a single parameter. The quantity β measures the relative tendency of the fingertip to bend globally rather than indent locally. Increasing the effective flexural rigidity $(EI)_{\text{eff}}$ decreases β, which suppresses global bending and shifts a larger fraction of the imposed displacement into local indentation. Conversely, decreasing $(EI)_{\text{eff}}$ increases β, so that more of the imposed displacement is absorbed by bending before substantial contact indentation develops.

In the limit of very large $(EI)_{\text{eff}}$, β becomes small and the solution approaches $\delta_c \approx \delta_{\text{total}}$, meaning that most of the imposed motion appears as local indentation. In the opposite limit, large β leads to greater global bending and reduced local indentation.

This immediately gives the model design value. Since the Hertz relation also gives the contact radius as $a = \sqrt{R_{\text{eff}} \delta_c}$, any design change that increases δ_c for a fixed imposed approach also increases the effective contact patch size predicted by the model. In this way, fingernail reinforcement and internal distal support influence contact behavior not only by making the fingertip stiffer in a generic sense, but by specifically shifting deformation into the contact mode that directly shapes force transmission and contact formation.

Of course, this model remains a reduced-order approximation. It is not intended to represent the richness of contact mechanics in real-world manipulation. Its value is different: by analytically coupling beam bending and Hertzian indentation, it isolates the mechanism by which a hybrid fingertip structure changes deformation partitioning. For fingertip design, this makes it possible to reason about how dorsal reinforcement and internal support alter contact formation before resorting to more computationally intensive analyses.

References

[1] S. Macenski, T. Foote, B. Gerkey, C. Lalancette, and W. Woodall, "Robot operating system 2: Design, architecture, and uses in the wild," *Science Robotics*, vol. 7, no. 66, eabm6074, 2022.